

Density Estimation via Measure Transport: Outlook for Applications in the Biological Sciences

Vanessa López-Marrero^{*,†,‡} Patrick R. Johnstone[§] Gilchan Park[†] Xihaier Luo[†]

September 28, 2023

Abstract

One among several advantages of measure transport methods is that they allow for a unified framework for processing and analysis of data distributed according to a wide class of probability measures. Within this context, we present results from computational studies aimed at assessing the potential of measure transport techniques, specifically, the use of triangular transport maps, as part of a workflow intended to support research in the biological sciences. Scarce data scenarios, which are common in domains such as radiation biology, are of particular interest. We find that when data is scarce, sparse transport maps are advantageous. In particular, statistics gathered from computing series of (sparse) adaptive transport maps, trained on a series of randomly chosen subsets of the set of available data samples, leads to uncovering information hidden in the data. As a result, in the radiation biology application considered here, this approach provides a tool for generating hypotheses about gene relationships and their dynamics under radiation exposure.

1 Introduction

The problem of estimating a probability distribution density from samples (e.g., observations, measurements, or simulation data) is ubiquitous in data science, uncertainty quantification, clustering and classification, and probabilistic modeling and inference tasks. Moreover, it is common among various scientific and engineering fields [30, 11, 1, 33, 5, 10, 31]. Often, well-known parametric density functions (dependent on few parameters), such as the Gaussian or Weibull density distribution functions, are adopted. While this may simplify certain tasks (e.g., computational ones), many of these known density distribution functions are not necessarily suitable for characterizing data that exhibit complex features, such as (spatial and/or temporal) correlations and non-Gaussian characteristics. Hence, a density estimation framework capable of characterizing a diverse range of properties is highly desirable. A measure transport approach [37, 29, 28] offers this possibility.

Optimal measure transport, broadly defined, deals with the problem of minimizing the cost of transporting one (probability) measure to another. The subject has a long history with significant impact in many fields of mathematics, such as probability theory, optimization, and partial differential equations, among others [37, 29]. Current interest on the topic stems from its potential in

*Corresponding author. E-mail: vlopezmar@bnl.gov

†Computational Science Initiative, Brookhaven National Laboratory

‡Institute for Advanced Computational Science (IACS), Stony Brook University.

§Work performed while at the Computational Science Initiative, Brookhaven National Laboratory. Current affiliation: Meta.

numerous areas, including density estimation, data science, machine learning, Bayesian inference, sampling, and data assimilation [1, 34, 33, 21, 6, 32, 28, 25, 9, 31, 38, 15]. Among various measure transport techniques under active research, we mention the use of triangular transport maps, normalizing/gradient flows, diffusion maps, and invertible neural networks. Although differing in the particulars, affording a unified framework for processing and analysis of data from a range of distributions (Gaussian, non-Gaussian, uni-modal, multi-modal, etc.) is a powerful property common to all.

In this paper we consider measure transport for density estimation from data, in particular the use of triangular transport maps, envisioning its potential within a computational workflow for tasks associated with biological applications. The motivating problem, which is density estimation (or prior/posterior construction) when data is scarce, as well as the proposed workflow, are described in Section 2. Overviews of the topics of measure transport and density estimation via triangular transport maps appear, respectively, in Sections 3 and 4. References for thorough treatments of these subjects are provided therein. Computational experiments performed using gene expression data are presented in Section 5.

2 Motivating Application

The present work stems from the conception of a comprehensive computational workflow intended to support research in the biological sciences, in particular the radiation biology domain. Within this effort, our interest is in enabling a *unified* framework where probabilistic modeling, inference, and statistical analyses can be carried out for a wide range of data distributions. As noted in the Introduction (Section 1), measure transport offers the possibility of such unified approach. We envision measure transport techniques comprising one component within the larger scope, as depicted in Figure 1.

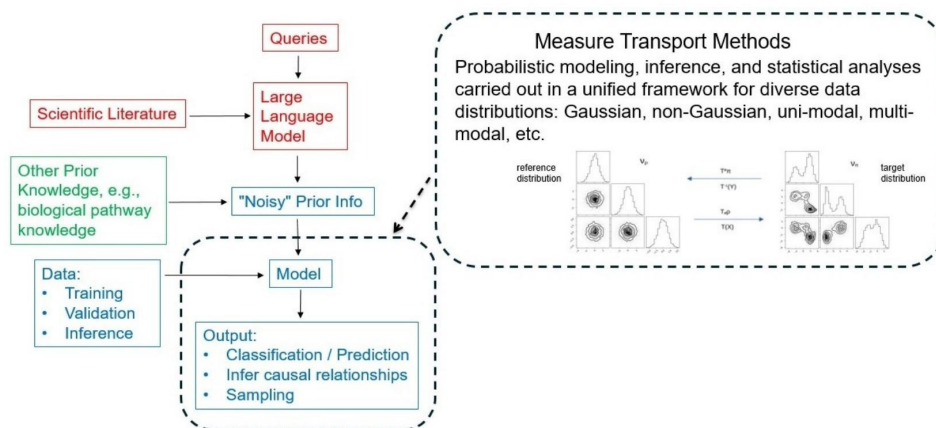


Figure 1: Computational workflow for probabilistic modeling, inference, and statistical analyses. To account for scarcity of data, model training can be augmented with prior knowledge. Such prior knowledge may come from large language models or human experts, for instance. Measure transport techniques allow for a unified framework for dealing with data exhibiting diverse characteristics.

One motivating problem within the framework from Figure 1 is that of probability distribution density estimation for phenotypic classification problems, for example, for inferring class labels, such as radiation exposure levels or cancer types, given sample data. Normalizing flows (one kind among the various measure transport methods) have been successfully used for clustering

and classification in the cancer domain [1]. Now, when data is scarce, regardless of the density estimation technique adopted, prior knowledge (associated with the particular application) may be used in conjunction with data to estimate the class-conditional densities. In the work [5], the authors proposed incorporation of prior knowledge from biological pathways for class-conditional density estimation as one approach for optimal Bayesian classifier design when data availability is limited. Here we also consider the use of prior knowledge from biological pathways, along with measure transport techniques, in the computational experiments reported in Section 5. In the workflow from Figure 1, we envision prior knowledge coming from other sources as well, such as large language models [26, 27] and human experts. This is the subject of future work.

The reader is referred to [11] for a thorough treatment of the topic of classification via probability density distribution functions (kernel density classification, per the terminology from [11]), among many other classification methods. We summarize next what is needed to make the discussions in Sections 4.2 and 5 (appearing later in the manuscript) self-contained. Assume we have K classes to infer sample membership from. Upon computing, separately, an estimated probability density distribution function π_j for each class C_j , $j = 1, \dots, K$, the probability $\Pr(C = k | \mathcal{Y} = y)$ that a given sample y belongs to class C_k can be obtained from the class-conditional densities $\{\pi_j\}_{j=1}^K$ via

$$\Pr(C = k | \mathcal{Y} = y) = \frac{\hat{\pi}_k \pi_k(y)}{\sum_{j=1}^K \hat{\pi}_j \pi_j(y)}, \quad (1)$$

where $\{\hat{\pi}_j\}_{j=1}^K$, $\sum_{j=1}^K \hat{\pi}_j = 1$, are estimates for the class prior probabilities. The latter may be determined from the proportion of training samples, for instance, or other prior knowledge.

Finally, in Section 5.2 we discuss how, as part of the computational framework from Figure 1, measure transport methods have the potential to address other problems, in addition to the above-mentioned classification one. More precisely, by uncovering information hidden in the data, adaptive transport maps [2] could provide a means for generating hypotheses regarding gene relationships for the radiation biology application considered in Section 5.2. Before getting into such details, we now continue with an overview of required topics from measure transport.

3 Basics of Measure Transport

As mentioned in the Introduction (Section 1), optimal measure transport addresses the problem of minimizing the cost of transporting one (probability) measure to another. We now give a summary of the basic concepts, as they relate to the problem of density estimation which is of interest to us. For a thorough treatment of the subject of measure transport, the reader may refer to [37, 29, 17, 4] (theory), [21, 28, 2] (computational), and references therein.

Informally, given two probability measures ν_ρ and ν_π defined on the algebra of Borel sets of \mathbb{R}^m , $m \geq 1$, and absolutely continuous with respect to the Lebesgue measure dx on \mathbb{R}^m , with densities ρ and π , respectively, an invertible map $T: \mathbb{R}^m \rightarrow \mathbb{R}^m$ transports ν_ρ to ν_π if and only if

$$\nu_\pi(B) = \nu_\rho(T^{-1}(B)) \quad (2)$$

for every Borel set $B \subset \mathbb{R}^m$. One says the map T pushes forward ν_ρ to ν_π , denoted $T_{\#}\nu_\rho = \nu_\pi$. Since we assume that both probability measures ν_ρ and ν_π are absolutely continuous with respect to the Lebesgue (volume) measure dx on \mathbb{R}^m , one may identify them with their probability densities ρ and π . That is, $\nu_\rho(dx) = \rho dx$ and $\nu_\pi(dx) = \pi dx$. Moreover, we restrict the class of maps T that we consider to the class of differentiable or even infinitely differentiable invertible maps. With

these assumptions one can write the measure transport equation (2) in terms of densities. Namely, the density ρ is the *pullback* $T^\# \pi$ of the density π ,

$$\rho(\cdot) = T^\# \pi(\cdot) = \pi(T(\cdot)) |\det J_T(\cdot)|, \quad (3)$$

where J_T is the Jacobian matrix of T . Conversely, the inverse T^{-1} of T pushes forward ν_π to ν_ρ , denoted $(T^{-1})_\# \nu_\pi = \nu_\rho$, and π is the pullback $(T^{-1})^\# \rho$ of ρ :

$$\pi(\cdot) = (T^{-1})^\# \rho(\cdot) = \rho(T^{-1}(\cdot)) |\det J_{T^{-1}}(\cdot)|, \quad (4)$$

where $J_{T^{-1}}$ is the Jacobian matrix of T^{-1} . An illustration of these fundamental concepts appears in Figure 2.

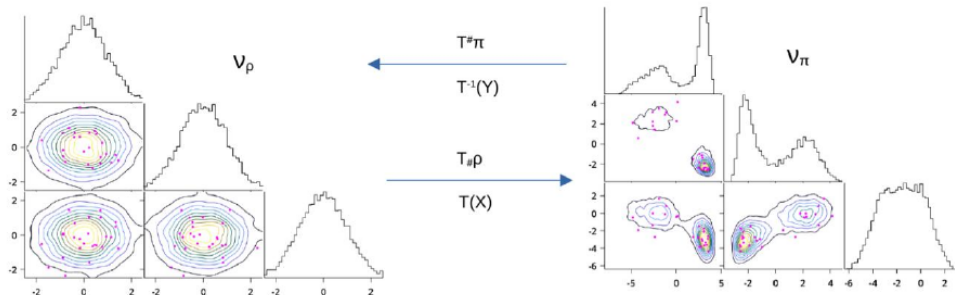


Figure 2: The map $T : \mathbb{R}^3 \rightarrow \mathbb{R}^3$ transports samples from ν_ρ , a multivariate standard normal (i.e., Gaussian), to samples from ν_π , a multivariate, multi-modal density distribution. The density ρ is the pullback $T^\# \pi$ of the density π . Conversely, the map T^{-1} transports samples from ν_π to samples from ν_ρ . The density π is the pullback $(T^{-1})^\# \rho \equiv T^\# \rho$ of the density ρ . Contour plots of the corresponding one- and two-dimensional marginal distribution densities also are shown.

Recall that we are concerned with the problem of estimating an unknown probability density function characterizing some given data set of samples or observations, for instance, gene expression data. Denote the corresponding unknown probability measure by ν_π and call it the *target* measure. On the other hand, let ν_ρ be a probability measure amenable to computations, for example, the standard normal $\mathcal{N}(0, I)$, so one can easily draw samples from it and evaluate its density ρ . Call this the *reference* measure. Now, let $\mathcal{X} = (\mathcal{X}_1, \mathcal{X}_2, \dots, \mathcal{X}_m)$ and $\mathcal{Y} = (\mathcal{Y}_1, \mathcal{Y}_2, \dots, \mathcal{Y}_m)$ be random vectors with probability distribution functions $F_{\mathcal{X}}$ and $F_{\mathcal{Y}}$, respectively, such that $dF_{\mathcal{X}} = \nu_\rho$ and $dF_{\mathcal{Y}} = \nu_\pi$. The random vectors \mathcal{X} , \mathcal{Y} assume, respectively, values $x, y \in \mathbb{R}^m$ (also denoted by $x \sim \nu_\rho$ and $y \sim \nu_\pi$). Then if $X = \{x \in \mathbb{R}^m : x \sim \nu_\rho\}$ and $Y = \{y \in \mathbb{R}^m : y \sim \nu_\pi\}$ are sets of samples formed from the values of the random vectors \mathcal{X} and \mathcal{Y} (i.e., the elements in X are distributed according to ν_ρ , and those in Y are distributed according to ν_π) the transport map should satisfy $\nu_\pi(Y) = \nu_\rho(T^{-1}(Y))$.

Thus, given the sets of samples X and Y , our goal is to *learn* (or compute) the transport map T and use it later as a predictor for the values of \mathcal{Y} (and therefore an estimator of ν_π). The set Y consists of samples (usually taken from experiment) of the random vector \mathcal{Y} distributed according to an *a priori unknown* target probability measure ν_π , while the reference probability measure ν_ρ is *a priori known* (e.g., Gaussian) and the set X is generated from samples of a random vector \mathcal{X} distributed according to ν_ρ . Under the assumption that one can compute such a map T transporting between the target and reference measures, the framework outlined herein and depicted in Figure 2 yields a method for approximating the desired unknown density function that characterizes the

given sample data set. Then, the central problem is to compute, or learn, such a map T . This problem is further addressed in Section 4.

Upon learning such a map T from data, evaluation of the (unknown) density π at a given (new) sample $y \sim \nu_\pi$ can be done via equation (4) as, by construction, all the functions on the right-hand side of equation (4) are known and can be evaluated. Moreover, because the reference measure is chosen to make sampling from it an easy and efficient task, sampling from the target measure can be done efficiently by drawing samples from the reference and transporting them to the target via the learned map T . Thus, probabilistic modeling, inference, and statistical analyses in the target space are enabled by such measure transport framework.

4 Transport Map Computation

To compute transport maps, we use software [36, 3] made available by the MIT Uncertainty Quantification (MUQ) Group [35]. The reader is referred to the original publications [8, 21, 32, 2] for complete descriptions of the numerical methods and software libraries. A summary is provided next, to make the present manuscript self-contained.

Let ν_ρ and ν_π be two (probability) measures defined on the algebra of Borel sets of \mathbb{R}^m , $m \geq 1$. Suppose that $T : \mathbb{R}^m \rightarrow \mathbb{R}^m$ is a transport map pushing forward ν_ρ to ν_π . That is, it satisfies the equation

$$\nu_\pi = T\# \nu_\rho \tag{5}$$

for T . By definition (see Section 3),

$$\nu_\rho = (T^{-1})\# \nu_\pi \tag{6}$$

also holds. The transport map T has m components

$$T_i(x_1, x_2, \dots, x_m), \quad i = 1, \dots, m, \tag{7}$$

and one has that $y_i = T_i(x_1, x_2, \dots, x_m)$, where $y = (y_1, y_2, \dots, y_m) \sim \nu_\pi$ and $x = (x_1, x_2, \dots, x_m) \sim \nu_\rho$. Conversely, the inverse transport map T^{-1} of T has m components

$$(T^{-1})_i(y_1, y_2, \dots, y_m), \quad i = 1, \dots, m, \tag{8}$$

and one has that $x_i = (T^{-1})_i(y_1, y_2, \dots, y_m)$.

A transport map T is computed via the solution of equation (5) and a minimization problem with cost or objective function $C_\rho(T)$ generally defined as

$$C_\rho(T) = \int_{\mathbb{R}^m} c(x, T(x)) \nu_\rho(dx). \tag{9}$$

The structure of the map T depends on ρ , π , and $c(\cdot, \cdot)$. Many types of maps (not necessarily optimal), or couplings, exist between measures [37, 28]. In this study we consider the use of triangular transport maps, as they enable practical numerical computation of a transport map and its inverse [21, 2].

4.1 Triangular Transport Maps

A transport map $T : \mathbb{R}^m \rightarrow \mathbb{R}^m$, $\nu_\pi = T_{\#}\nu_\rho$, is *triangular* if

$$y_i = T_i(x_1, x_2, \dots, x_i), \quad i = 1, \dots, m. \quad (10)$$

In other words, the i -th component T_i of a triangular transport map T only depends on the values $\{x_k\}_{k=1}^i$ of the first i random variables $\{\mathcal{X}_k\}_{k=1}^i$. Thus, the map components are

$$T(x) = \begin{bmatrix} T_1(x_1) \\ T_2(x_1, x_2) \\ T_3(x_1, x_2, x_3) \\ \vdots \\ T_m(x_1, x_2, \dots, x_m) \end{bmatrix}. \quad (11)$$

Conversely,

$$x_i = (T^{-1})_i(y_1, y_2, \dots, y_i), \quad i = 1, \dots, m. \quad (12)$$

To ensure positivity of the densities (3) and (4), each map component T_i in equation (10) must be differentiable with respect to x_i , and it must hold that $\partial_{x_i} T_i > 0$, for every $i = 1, \dots, m$. We refer to the latter as the class of increasing triangular maps. Similarly, each component $(T^{-1})_i$ (12) of the inverse map T^{-1} of T must satisfy said properties with respect to the variables y_i [4, 21]. Furthermore, when both ν_ρ and ν_π are absolutely continuous with respect to the Lebesgue measure dx on \mathbb{R}^m with densities ρ and π , respectively, if $c(x, T(x)) = \|x - T(x)\|^2$, where $\|\cdot\|$ is the Euclidean distance on \mathbb{R}^m , and ν_ρ is Gaussian, instead of (9) one may seek to minimize the relative entropy, or Kullback-Leibler divergence,

$$\mathrm{D}_{\mathrm{KL}}(\nu_\pi \| \nu_\rho) = \int_{\mathbb{R}^m} \pi \log(\pi/\rho) dx = \mathbb{E}_\pi(\log(\pi/\rho)), \quad (13)$$

as $C_\rho(T) \leq 2A \mathrm{D}_{\mathrm{KL}}(T_{\#}\nu_\rho \| \nu_\rho)$, where $A > 0$ is a constant [24, 17, 4]. Under the assumption that the map T is differentiable or even smooth, one may also look at the problem of computing an optimal transport map T as a solution of the optimization problem $\arg \min_T C_\rho(T)$ (or $\arg \min_T \mathrm{D}_{\mathrm{KL}}(T_{\#}\nu_\rho \| \nu_\rho)$) under the partial differential equation constraint (3) for the map T .

Triangular maps enable efficient numerical computation of a transport map and its inverse, which is also triangular. Moreover, triangular transport maps are well-suited for conditional density estimation and sampling [8, 21, 32, 2, 15]. Techniques for computational efficiency and scalability to high-dimensional problems include, among others, composition of low order maps [8] and the use of *sparse triangular transport maps* [22, 32, 2, 15]. For such sparse maps, any given map component $(T^{-1})_i$ in equation (12) may depend only on a proper subset (possibly empty) of the variables $\{y_j\}_{j=1}^{i-1}$ and on y_i . Dependence on y_i is required. A *diagonal map*, in particular, has $x_i = (T^{-1})_i(y_i)$ for each $i = 1, \dots, m$. The random variables that a given map component depends on is referred to as the set of active variables for the map component. Collectively, they define a sparsity pattern for the transport map. For a summary of these notions, see Figure 3.

Sparse triangular transport maps can be computed without a sparsity pattern specified a priori, using specially designed algorithms which have been shown to perform well for density estimation problems even when sample data is limited in amount [2]. Alternatively, a desired sparsity pattern could be specified explicitly and enforced when computing a transport map. As discussed in Section 2, one motivation for our research is density estimation from samples when available data is scarce. We hence consider sparse maps for our motivating application, as expanded upon in Section 5 further below. Next, we conclude the current Section 4 with some brief comments on density estimation via triangular transport maps and several illustrative examples.

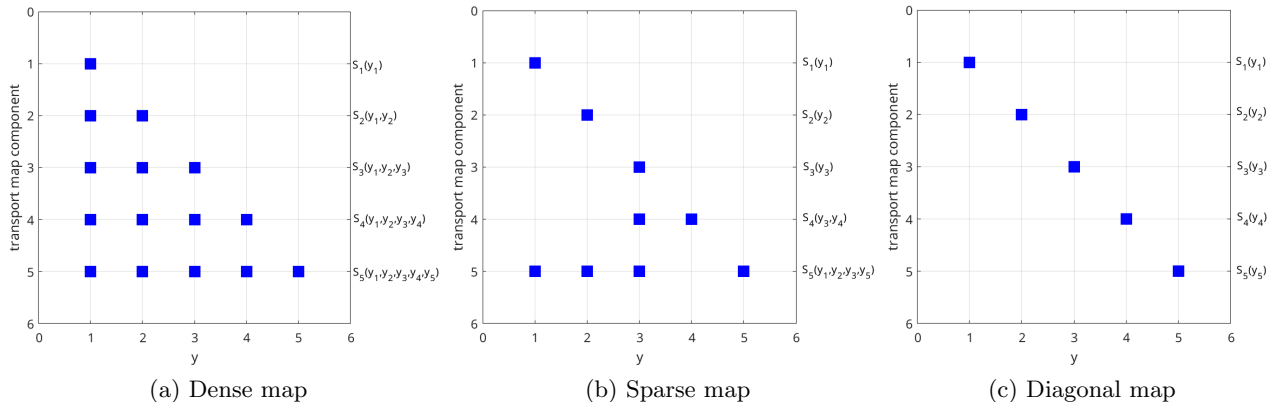


Figure 3: Pictorial representation of triangular transports maps. To simplify notation in subplots 3a–3c, we denote $S \equiv T^{-1}$ for the transport map T^{-1} from (12). In this example, $S : \mathbb{R}^5 \rightarrow \mathbb{R}^5$. In each plot, the horizontal axis indexes the random variables $\{\mathcal{Y}_k\}_{k=1}^5$ and the vertical axis indexes the map components $\{S_i\}_{i=1}^5$. A square appears at the intersection of grid point (k, i) if the i -th map component S_i depends on the value y_k of the k -th random variable \mathcal{Y}_k . For any given map component, the set of *active variables* is the set of random variables that the map component depends on. Collectively, the active variables define a sparsity pattern for the transport map.

4.2 Density Estimation from Data

Referring to equations (5)–(6), recall from Section 3 that we designate the probability measure ν_ρ as the reference measure and the probability measure ν_π as the target measure. The target density π is unknown, but samples from the target measure ν_π are available. On the other hand, the reference measure ν_ρ is chosen to be known and so that it is amenable to computations and sampling. The reference measure is often selected to be the standard normal $\mathcal{N}(0, I)$, and that is our choice in all of our experiments.

Given a set of samples from the target measure ν_π , we use software libraries [36, 3] made available by the MIT Uncertainty Quantification (MUQ) Group [35] to compute a transport map (and its inverse) between the unknown target and reference measures. The transport map is computed as the solution of an optimization problem with objective function (13), using the Sample Average Approximation (SAA) algorithm. The reader is referred to [21] for full details.

Upon computation of the transport map, the target density π can be evaluated via equation (4). Given a (new) sample $y \sim \nu_\pi$, the value $\pi(y)$ can thus be obtained and used as needed, for instance for the classification problem from our motivating application, which was described in Section 2. The MUQ software libraries [36, 3] provide functionality for evaluating the target density, among many other capabilities.

To describe an application of the measure transport framework, in Figure 4 are displayed computed approximations to density functions for univariate measures. The triangular transport maps for these approximations were computed using the TransportMaps library [36], version 2.0b3. The figure shows how the measure transport framework can be used for uni-modal and multi-modal data distributions alike. Further details are provided in the caption for Figure 4.

Finally, transport map approximations to densities for a multivariate data set chosen from the UC Irvine Machine Learning Repository [16] appear in Figure 5. Although not from the biological domain, we selected the data set [18] because it yielded a good, non-contrived example for illustrating the benefits of a measure transport approach to density estimation. The data set was

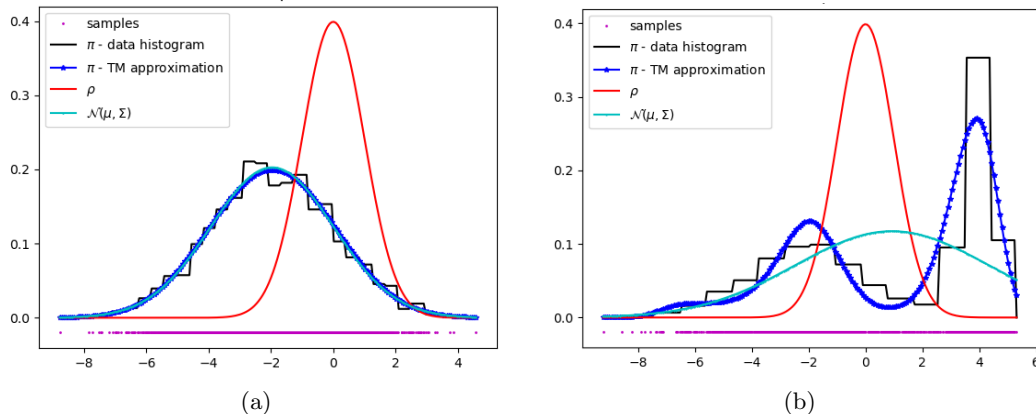


Figure 4: Approximations to univariate density functions via triangular transport maps. In each of the subplots 4a and 4b, (i) the red curve is the reference density ρ – a standard normal, (ii) a histogram of samples from the target density π is depicted with black lines, (iii) the blue curve is the transport map (TM) approximation to the target density π , and (iv) the cyan curve is the density for the normal distribution $\mathcal{N}(\mu, \Sigma)$ with mean and standard deviation being that of the sample data. For 4a, the data set was created by drawing samples from a normal distribution $\mathcal{N}(\mu, \Sigma)$ with $\mu \neq 0$ and $\Sigma \neq 1$. The TM approximation to the target density agrees with that of the true density. The samples for the data set from 4b are from a multi-modal distribution. The resulting TM approximation to the target density reflects this and follows the data histogram more closely, as opposed to the density for $\mathcal{N}(\mu, \Sigma)$.

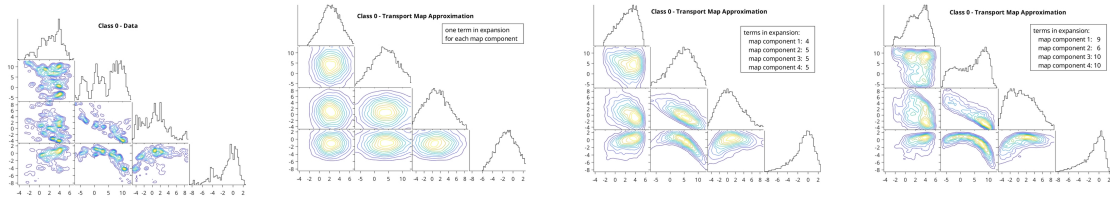
created from images taken from genuine and forged banknote-like specimens, creating two classes for classification problems. For the purpose of discussion, we identify them as Class 0 and Class 1 and compute approximations to the densities for each of the two classes. The triangular transport maps for the approximated densities were obtained using the AdaptiveTransportMaps library [3], which allows for computing adaptive parameterizations of transport maps [2].

We refer the reader to the original publication [2] for complete details, but note here that among the several parameters defining such *adaptive transport maps* is the number of terms in the basis function expansion for each map component. Figure 5 illustrates the effect of varying this allowed maximum number of terms and shows that, for each of the Class 0 and Class 1 data, increasingly good approximations to the density can be obtained. Classification results obtained via the transport map approximated density distribution functions are also shown. For comparison, classification results obtained using several Matlab classifiers [12] are included in Figure 5 as well.

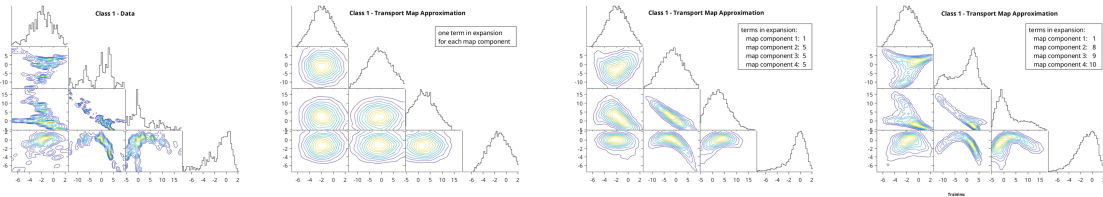
5 Application to Gene Expression Data

To conduct an initial assessment of the potential of measure transport techniques for phenotypic classification within the radiation biology domain, we use the GSE43151 data set [23] available from the Gene Expression Omnibus (GEO) database [7], as in previous work [19, 20]. This data set contains gene expression data for 121 human blood samples, some with zero exposure to radiation, and others exposed to low-dose radiation or high-dose radiation. Out of the total number of samples, 18 are in the zero-dose category, 87 are in the low-dose category, and 16 are in the high-dose category. For more details on the GSE43151 data set, the reader may refer to [23].

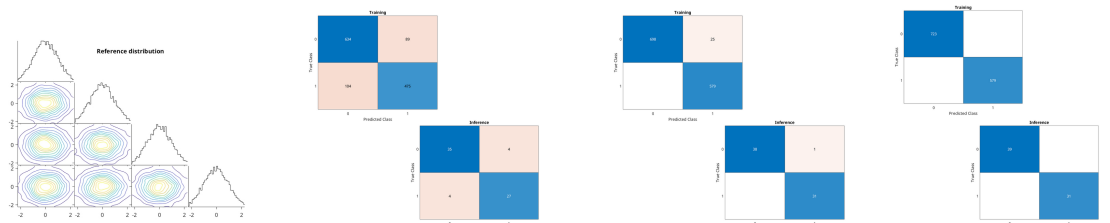
Genes correspond to the random variables jointly distributed according to the unknown target



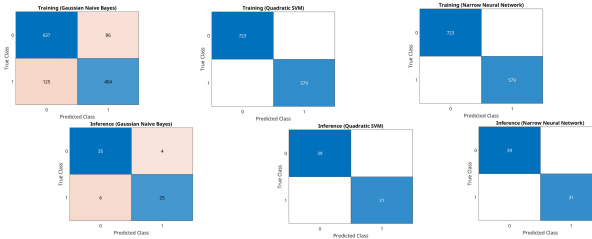
(a) Class 0



(b) Class 1



(c) Transport maps reference probability density (left); confusion matrices (middle and right) from classification results using the class-conditional density approximations from 5a and 5b



(d) Confusion matrices for naive Bayes (left), support vector machine (middle), and neural network (right) classification results

Figure 5: Transport map approximations to the class-conditional densities for the data set [18]. *Subplot 5a*: Class 0 marginal distribution densities from data (left) and different transport map approximations (middle and right), with an increasing number of terms in the basis function expansions for the transport map components. Clearly, the data density distribution is not Gaussian. The first transport map approximation, with only one term in the aforementioned basis function expansion, does a poor job at approximating the target density. The accuracy of the density approximation improves with an increased number of terms in the basis function expansions. *Subplot 5b*: As in subplot 5a, but for Class 1. *Subplot 5c*: Shown on the left is the reference probability density, which is a standard multivariate normal for all transport map approximations. Afterwards: improved classification result as the accuracy of the density approximations increases. The top confusion matrices are from training data and the bottom confusion matrices are from inference data. *Subplot 5d*: As the data is not Gaussian, a naive Bayes classifier (left) performs poorly. A support vector machine (middle) and neural network (right) classifier perform as well as the classification resulting from the most accurate transport maps approximation (right, subplots 5a-5c).

probability densities we seek to estimate. For feature (i.e., random variables) selection, we consider genes in biological pathways relevant to the GSE43151 data set, as determined by the pathway ranking procedure from [19, 20]. As previously mentioned in Section 4.1, we investigate two different measure transport techniques, namely, explicitly enforcing sparsity patterns in the transport maps and adaptive transport maps. Details appear in Section 5.1 for the former approach and in Section 5.2 for the latter one. In each case, the resulting transport maps are sparse, as defined towards the end of Section 4.1 and depicted in Figure 3.

As discussed next in Section 5.1 below, prior knowledge extracted from known biological pathways, such as relationships among genes, could be used to fix sets of active variables (i.e., sets of variables that the map components depend on) when computing the sparse transport maps. This is advantageous computationally, particularly if the extracted relationships are known with (reasonable) certainty. However, this approach could end up being biased and too restrictive (for example, missing possible dependencies between genes that are a priori unknown as well as obscuring their change when exposed to radiation). Hence, in Section 5.2, we also consider adaptive transport maps without any a priori imposed restrictions on the sparsity patterns of their components. With the latter class of maps, via specifically designed algorithms [2], sparse transport maps can be constructed and computed without the need to fix the set of active variables a priori. For our application, adaptive transport maps may thus offer more flexibility and would be more advantageous when prior knowledge about gene relationships is lacking or uncertain.

5.1 Prescribed Sparsity Patterns from Gene Relationships

One simple way to incorporate prior information into transport map construction is by building a sparse transport map using knowledge of the dependence structure of the set of random variables under consideration. If the random variables adhere to a Bayesian network, then the active variables of the transport map may be obtained from this network in a straightforward way [32]. In doing so, the number of parameters that need to be fit can be significantly reduced compared with triangular and dense maps.

For the gene expression data under radiation exposure, we used the Kyoto Encyclopedia of Genes and Genome (KEGG) database [14] to extract Bayesian networks describing the relationships between the genes for a given pathway. While KEGG provides a variety of relationships between genes, we focused on protein-protein (PPrel) activation and inhibition relationships. In particular, if there was a directed edge from gene A to gene B in the KEGG graph of type PPrel-activation/inhibition, then an edge from A to B was added to the Bayesian network. We also added edges between genes that are part of a gene complex. This information was extracted from KEGG Markup Language (KGML) files and read into Python using the BioPython package. We only consider pathways that resulted in directed acyclic graphs (DAGs) under these PPrel relationships. Software to extract this information is available from [13]. The transport maps for the experiments reported in this section were computed using the TransportMaps library [36], version 2.0b3.

To test out the performance of the sparse transport maps framework within this context, we selected 5 gene pathways from the KEGG database that performed well on the pathway activation scoring performed in [20] and resulted in DAGs as well, through the above analysis. We considered the following pathways: hsa05131, hsa04714, hsa04658, hsa05166, and hsa04650. We performed the classification task of discriminating zero-dose versus low-dose samples using the subset of genes corresponding to each pathway. We were interested in the small-data regime where prior information can provide the biggest benefit, so we used only 25% of the data for the training set and the rest for evaluation, resulting in 25 training data samples and 80 test samples. Since there is so little data in the zero-dose case (only 4 training samples) it makes sense to use a diagonal transport map

for this case, while other approaches performed poorly. In the low dose-case, there are 21 training samples and we consider using the following maps:

- *Diagonal map*: The i -th component of the transport map T^{-1} from equation (12) only depends on the value y_i of the i -th random variable \mathcal{Y}_i .
- *Dense triangular map*: The i -th component of the transport map T^{-1} depends on the values $\{y_j\}_{j=1}^i$ of the random variables $\{\mathcal{Y}_j\}_{j=1}^i$.
- *KEGG-informed sparse map*: The i -th component of the transport map T^{-1} depends on the value y_i of the random variable \mathcal{Y}_i and the values of a proper subset Z_i (possibly empty) of the random variables $\{\mathcal{Y}_j\}_{j=1}^{i-1}$. For the experiments reported here, $Z_i = \emptyset$ typically. The set of active variables for each map component is derived from biological prior knowledge in the form of a topological sort of the KEGG graph [13].

Refer to Figure 3 for a pictorial representation of the above listed types of maps. In each of the above cases, we have $T^{-1}: \mathbb{R}^m \rightarrow \mathbb{R}^m$, where m is the number of genes extracted from the pathway.

Figure 6 displays the F_1 score averaged over both classes for each of the pathways and each method including Naive Bayes as a baseline. From the plot, we see that transport maps with the sparsity pattern derived from prior knowledge provides an improvement in performance across all pathways except one. Note the poor performance of the dense triangular map, which is unable to fit such a small amount of data.

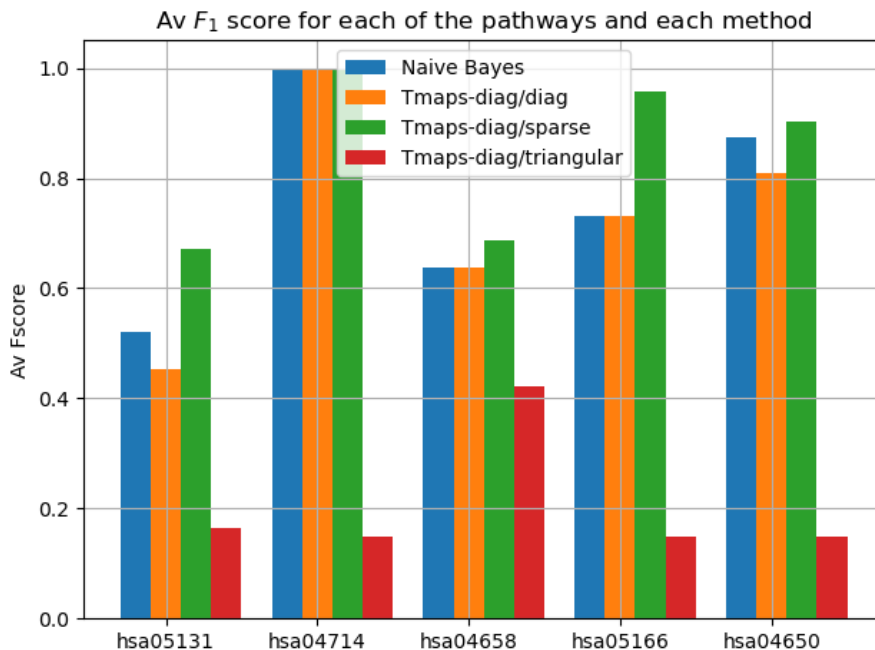


Figure 6: Classification results with KEGG-informed sparse transport map

5.2 Adaptive Transport Maps

We now move on to adaptive transport maps, for which transport map sparsity patterns (i.e., the dependence structure of the set of random variables jointly distributed according to the target

probability density) are not being prescribed a priori. To design experiments for this approach, we selected two pathways from the KEGG database [14], namely pathways hsa04120 and hsa05202. This was based on the pathway ranking procedure from [20], using the GSE43151 data set, where pathway hsa04120 ranked as the top pathway showing significant differential activation in response to low-dose radiation, as compared to zero-dose, and pathway hsa05202 ranked as the top pathway showing significant differential activation in response to high-dose radiation, as compared to zero-dose. The GSE43151 data set contains samples for 10,874 genes. After accounting for genes present in both the GSE43151 data set and in the selected pathways, we were left with 108 genes for pathway hsa04120 and 98 genes for pathway hsa05202.

Within the context of the classification problem from Section 2, we performed two groups of experiments. The first was for classifying samples between zero-dose (Class 0) and low-dose (Class 1) radiation, using the set of 108 genes common to both the GSE43151 data set and the hsa04120 pathway to define the set of random variables for the class-conditional densities. In the second group of experiments, classification was between zero-dose (Class 0) and high-dose (Class 1) radiation, using the set of 98 genes common to both the GSE43151 data set and the hsa05202 pathway as the set of random variables. For each of these two ‘‘Class 0 - Class 1 scenarios’’ we then decided on a number of maximum terms allowed in the basis function expansion for each map component (see the end of Section 4.2) and, given a maximum number of terms allowed (more on our choices later), a sequence of runs, say N of them, was carried out. For each of these runs:

1. A random ordering of the data samples from the GSE43151 data set was performed.
2. For each of Class 0 and Class 1, the first half of the samples from the resulting ordering was selected as a training data set and the second half was withheld for inference.
3. An adaptive transport map approximation to each class-conditional density was computed.
4. Classification was done, per (1), using the resulting class-conditional densities and the samples held for inference.
5. For comparison, classification was done with Matlab’s naive Bayes and support vector machine classifiers using the same training and inference data sets from item 2 above.

This is formally described in Algorithm 1, using the mathematical notation introduced previously in Section 3.

Results from the above described runs are summarized in the form of F_1 scores for the classification results. These are shown in Figure 7 for the case when Class 0 and Class 1 were set, respectively, as the zero-dose and low-dose radiation classes. For the zero-dose and high-dose classification scenario, results are summarized in Figure 8. We note that for the experiments conducted, all classifiers ended up performing well. This was the case also in other preliminary experiments with the selected GSE43151 data set. A small number of terms (1-2 for the zero- and high-dose radiation classes; 1-6 for the low-radiation class) in the adaptive transport maps basis function expansions were sufficient for the approximations. Varying the maximum number of allowed terms in the transport maps basis function expansions did not yield appreciable differences in the results, contrary to the (non-biology) example from Figure 5. However, our experiments (as previous works from others) illustrate that the same measure transport framework can be used successfully (in practice) for diverse data sets.

Furthermore, as shown in the original publication [2], adaptive transport maps approximations can reveal (unknown) dependence structure among the set of random variables jointly distributed according to the target probability density. Thus, adaptive transport maps have the potential to

Algorithm 1 Classification experiments with adaptive transport maps and GSE43151 data set

Notation:

N : total number of runs

$m \geq 1$: number of genes in the subset of genes extracted from the GSE43151 dataset

$y \in \mathbb{R}^m$: values (gene expression data) of a random vector $\mathcal{Y} = (\mathcal{Y}_1, \mathcal{Y}_2, \dots, \mathcal{Y}_m)$

K : number of classes

π_k : (unknown) target probability density for Class $k \in \{0, \dots, K - 1\}$

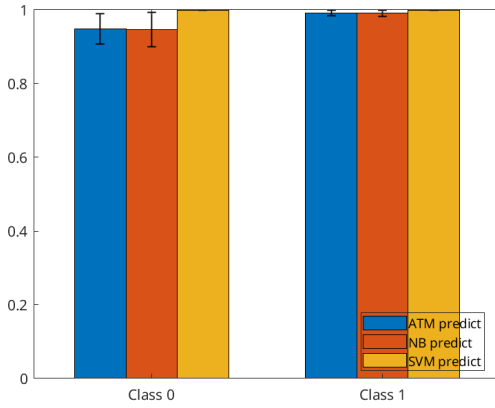
$Y_k = \{y \in \mathbb{R}^m : y \sim \nu_{\pi_k}\}$: set of all samples available for Class $k \in \{0, 1, \dots, K - 1\}$

$n_k = \text{Card}(Y_k)$: number of samples in Y_k , $k \in \{0, 1, \dots, K - 1\}$

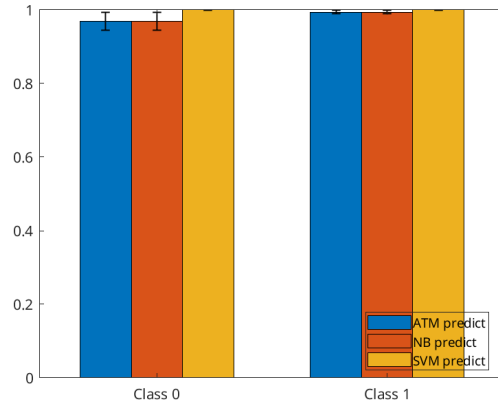
\mathcal{S}_{n_k} : group of permutations on n_k elements, acting on Y_k , with $\text{Card}(\mathcal{S}_{n_k}) = n_k!$

Algorithm:

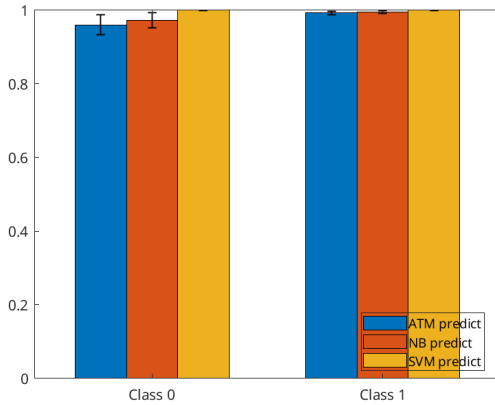
- 1: **for** $n = 1$ to N **do**
 - 2: **for** each $k \in \{0, 1, \dots, K - 1\}$ **do**
 - 3: Choose an order on the set Y_k
 - 4: Choose randomly an element $\sigma \in \mathcal{S}_{n_k}$.
 - 5: Compute $\sigma(Y_k)$, i.e., act on Y_k by σ and reorder it.
 - 6: Split the set $\sigma(Y_k) = \sigma(Y_k)^{\text{tr}} \sqcup \sigma(Y_k)^{\text{inf}}$ along this order into a disjoint union of the set $\sigma(Y_k)^{\text{tr}}$ of its first $\lfloor \frac{n_k}{2} \rfloor$ elements (designated as the training set) and the set $\sigma(Y_k)^{\text{inf}}$ of the remaining $n_k - \lfloor \frac{n_k}{2} \rfloor$ elements (designated as the inference set).
 - 7: Compute an adaptive transport map approximation T_k from the reference ρ to the target density π_k using only $\sigma(Y_k)^{\text{tr}}$ as a training set. That is, T_k is computed to satisfy the condition $\nu_{\pi_k}(\sigma(Y_k)^{\text{tr}}) = \nu_{\rho}(T_k^{-1}(\sigma(Y_k)^{\text{tr}}))$. (cf. equation (2))
 - 8: **end for**
 - 9: **for** each $k \in \{0, 1, \dots, K - 1\}$ **do**
 - 10: Compute $\hat{\pi}_k = \lfloor \frac{n_k}{2} \rfloor / \sum_{s=0}^{K-1} \lfloor \frac{n_s}{2} \rfloor$, the estimates for the class prior probabilities. (cf. equation (1))
 - 11: **end for**
 - 12: **for** each $k \in \{0, 1, \dots, K - 1\}$ **do**
 - 13: **for** each $y \in \sigma(Y_k)^{\text{inf}}$ (the inference set) **do**
 - 14: Compute the probability $\Pr(C = k | \mathcal{Y} = y) = \hat{\pi}_k \pi_k(y) / \sum_{s=0}^{K-1} \hat{\pi}_s \pi_s(y)$ that sample y belongs to Class k (cf. equation (1)), where $\pi_s(y)$ is estimated via equation (4) using the already computed (in step 7 above) transport map T_s , for each $s \in \{0, 1, \dots, K - 1\}$.
 - 15: **end for**
 - 16: **end for**
 - 17: (Optional) For comparison, compute classification with Matlab's naive Bayes and support vector machine classifiers using the same training and inference data sets from step 6 above.
 - 18: **end for**
-



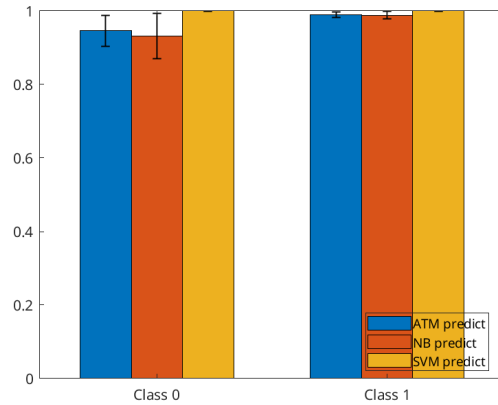
(a) Averaged F_1 scores, all experiments



(b) Averaged F_1 scores, subset of 20 experiments. Maximum number of terms allowed in ATM basis function expansions: 1 for Class 0, 1 for Class 1.

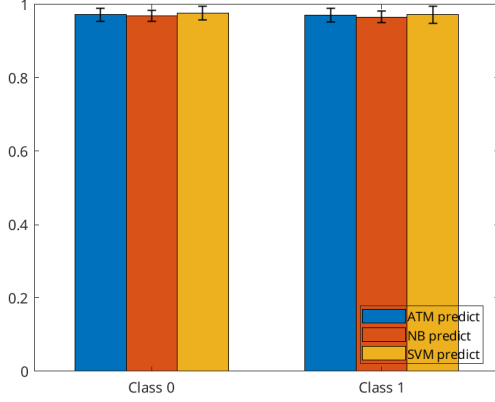


(c) Averaged F_1 scores, subset of 20 experiments. Maximum number of terms allowed in ATM basis function expansions: 2 for Class 0, 5 for Class 1.

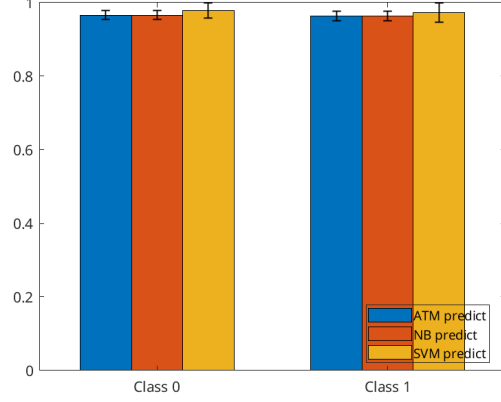


(d) Averaged F_1 scores, subset of 20 experiments. Maximum number of terms allowed in ATM basis function expansions: 2 for Class 0, 6 for Class 1.

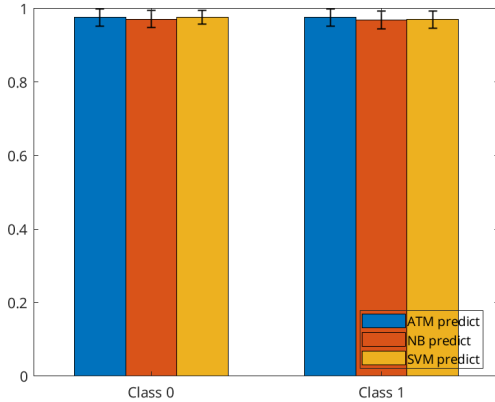
Figure 7: Summary of classification results from adaptive transport maps (ATM) approximations to the class-conditional densities, naive Bayes (NB) classifier, and support vector machine (SVM) classifier. Class 0 is zero-dose radiation; Class 1 is low-dose radiation. The available number of samples were 18 for Class 0 and 87 for Class 1. For each experiment (i.e., run), the available samples were divided randomly into 50% for training and 50% for inference. The total number of experiments was 100. For this data set, all methods performed well, with SVM achieving perfect results in most experiments. On average, the classification results were equal for the ATM density approximations and for naive Bayes, as seen in subplot 7a. For disjoint subsets of experiments (subplots 7b-7d), the ATM and naive Bayes classifications performed equally, or one better than the other. For all experiments, classification results were more accurate for Class 1. This is not surprising, since there were more data samples available for Class 1.



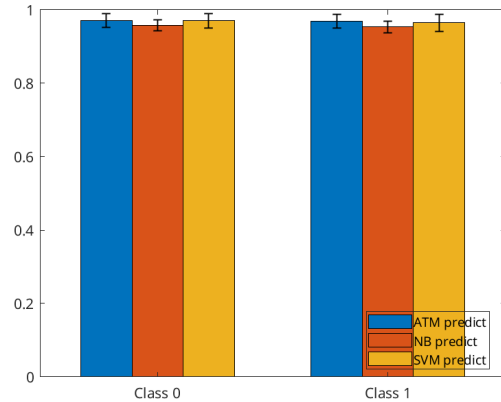
(a) Averaged F_1 scores, all experiments



(b) Averaged F_1 scores, subset of 20 experiments. Maximum number of terms allowed in ATM basis function expansions: 1 for Class 0, 1 for Class 1.



(c) Averaged F_1 scores, subset of 20 experiments. Maximum number of terms allowed in ATM basis function expansions: 2 for Class 0, 1 for Class 1.



(d) Averaged F_1 scores, subset of 20 experiments. Maximum number of terms allowed in ATM basis function expansions: 2 for Class 0, 2 for Class 1.

Figure 8: Summary of classification results from adaptive transport maps (ATM) approximations to the class-conditional densities, naive Bayes (NB) classifier, and support vector machine (SVM) classifier. Class 0 is zero-dose radiation; Class 1 is high-dose radiation. The available number of samples were 18 for Class 0 and 16 for Class 1. For each experiment (i.e., run), the available samples were divided randomly into 50% for training and 50% for inference. The total number of experiments was 100. For this data set, all methods performed well, and nearly equal, on average. Classification scores were around the same for Class 0 and Class 1.

serve as tools for scientific discovery. For our radiation biology application, a natural question would then be whether the sparsity patterns resulting from the transport maps approximations to the target densities contain or reveal any biological information, for example, relationships between the genes associated with the transport map sparsity patterns. This is another task within the framework introduced in Section 2 (see Figure 1), independent of the classification problem, where the measure transport approach can have an impact.

For instance, the sparsity pattern shown in Figure 3b resulted from the computation of the transport maps needed for estimating the class-conditional density for low-dose radiation, using a subset of five genes from the GSE43151 data set as the random variables jointly distributed according to the target measure. From the sparsity pattern in Figure 3b, one question that arises naturally is whether within the radiation biology domain there are known relationships that correspond to the exhibited sparsity pattern, or whether there may exist unknown relationships, among the genes associated with random variables \mathcal{Y}_3 and \mathcal{Y}_4 or between the genes associated with the random variables \mathcal{Y}_1 , \mathcal{Y}_2 , \mathcal{Y}_3 and \mathcal{Y}_5 . Thus there is potential for hypotheses generation and subsequent expert verification. In addition, within the context of the computational workflow from Figure 1, the resulting sparsity patterns may conceivably be useful for designing queries (regarding gene relationships) for large language models as well [26, 27].

Now, given sufficient data samples, one can expect that sparsity patterns resulting from adaptive transport map density approximations to the data distribution will accurately uncover dependencies or associations hidden in the data. But even when data is scarce one may be able to use such sparsity patterns for hypotheses generation. Namely, one can gather statistics by computing many adaptive transport map density approximations using different (randomly selected) subsets of the data as training sets, and then identifying common dominating patterns appearing in the resulting collection of transport map sparsity patterns. This line of research is among our ongoing work. We discuss it next and in Figures 9–12, where results are shown from our ongoing computational experiments. In order to develop some intuition into the dependence structure of the genes from the GSE43151 data set, without assuming any knowledge that fixes the set of transport map active variables a priori, we consider a subset of six genes from the GSE43151 data set as the random variables jointly distributed according to the unknown target measure. That is, in what follows, $T^{-1}: \mathbb{R}^6 \rightarrow \mathbb{R}^6$ in equation (12).

Recall from Figure 3 that in our pictorial representation of transport map sparsity patterns, the horizontal axis indexes the random variables $\{\mathcal{Y}_k\}_{k=1}^6$ and the vertical axis indexes the map components $\{(T^{-1})_i\}_{i=1}^6$. A square appears at the intersection of grid point (k, i) if the i -th map component $(T^{-1})_i$ depends on the value y_k of the k -th random variable \mathcal{Y}_k . For any given map component, the set of active variables is the set of random variables that the map component depends on. The active variables define a sparsity pattern for the transport map. We emphasize again that the adaptive transport map computation methods from [2] determine the set of active variables, without specification of it prior to computing the transport map.

Due to the small number of total samples available in the GSE43151 data set, sparsity patterns resulting from adaptive transport map approximations to the target measure may differ when different subsets of the total samples set are used to compute the transport maps. Figure 9 exemplifies this for the zero-dose and low-dose radiation classes. However, we hypothesize that statistics collected from various runs may nevertheless allow for uncovering information hidden in the data.

As in Algorithm 1, we work with subsets (as training sets) extracted from the set of data samples after random permutations of the ordered set of GSE43151 data samples. For each of the zero-dose and low-dose radiation classes, we computed the frequency with which each random variable appeared in the set of active variables after computing an adaptive transport map approximation to the target measure, for a given number of such training subsets (equal to the number of runs N

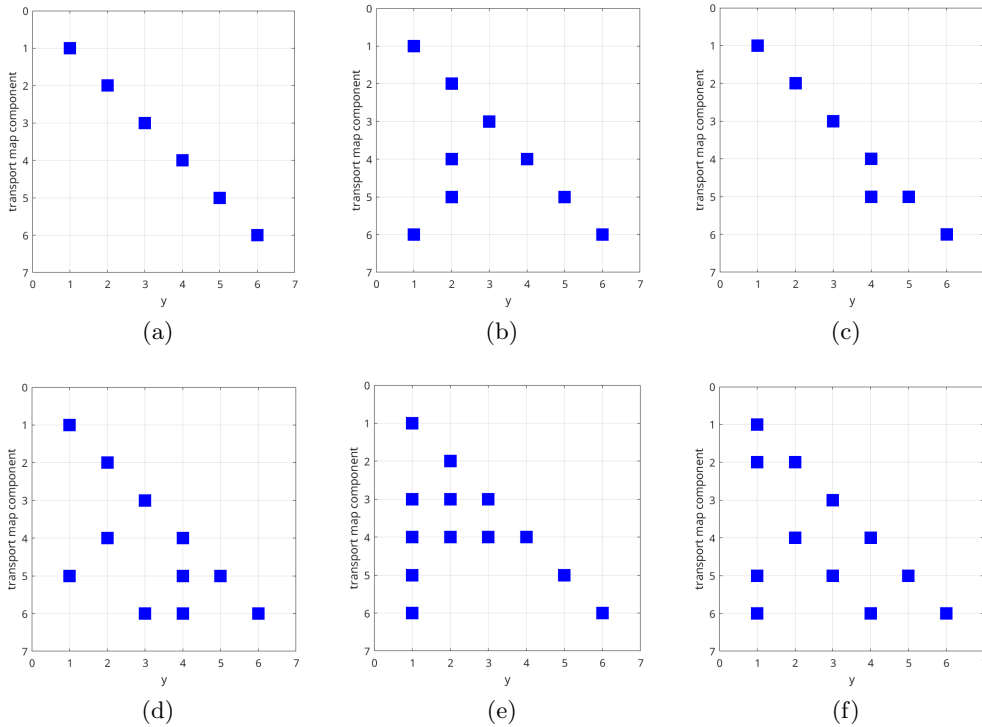


Figure 9: Due to the small number of total samples available, resulting transport map sparsity patterns may differ when different subsets of the total samples set are used to compute adaptive transport maps. Subplots 9a–9c exemplify this for three select subsets (of 9 samples each) from the zero-dose radiation class. Similarly for the low-dose radiation class in subplots 9d–9f, where each subset had 44 samples when computing the corresponding adaptive transport map. Statistics collected from various runs may nevertheless allow for uncovering information hidden in the data, as shown in Figures 10–12.

for each one of the classes). Results are shown in Figures 10 and 11, respectively, for the zero-dose and low-dose radiation classes.

To explain the pictorial representation of such “aggregated” sparsity patterns, let’s take one subplot from Figure 10, for example, subplot 10a. Note the grid point ordering on the plot axes: left to right for the horizontal axis, indexing the random variables $\{\mathcal{Y}_k\}_{k=1}^6$, and top to bottom for the vertical axis, indexing the map components $\{(T^{-1})_k\}_{k=1}^6$. The plot color bar ranges from 1 to the total number of data subsets considered, which in this case was 10. Since, for each $i = 1, \dots, 6$, the i -th map component $(T^{-1})_i$ must depend on the value y_i of the i -th random variable \mathcal{Y}_i , and we are aggregating results for 10 data subsets, the frequency count depicted on each of the diagonal grid points is 10. Thus, each square on a diagonal grid point is identified with the highest frequency, per the color bar. Out of the 10 transport maps computed (one for each of the 10 data subsets), three resulted with the 4-th map component having dependence on the value y_2 of the random variable \mathcal{Y}_2 . Hence the square at grid point (2,4) is identified with a frequency of 3, per the color bar. Similarly, two out of the 10 transport maps resulted with dependence on the value y_1 of the random variable \mathcal{Y}_1 for the 6-th map component and therefore the square at grid point (1,6) is identified with a frequency of 2. Finally, there were three instances of aggregated dependence with frequency of 1. These are identified by the white squares (lowest frequency per the color bar) appearing at grid points (1,5), (1,2), and (4,5).

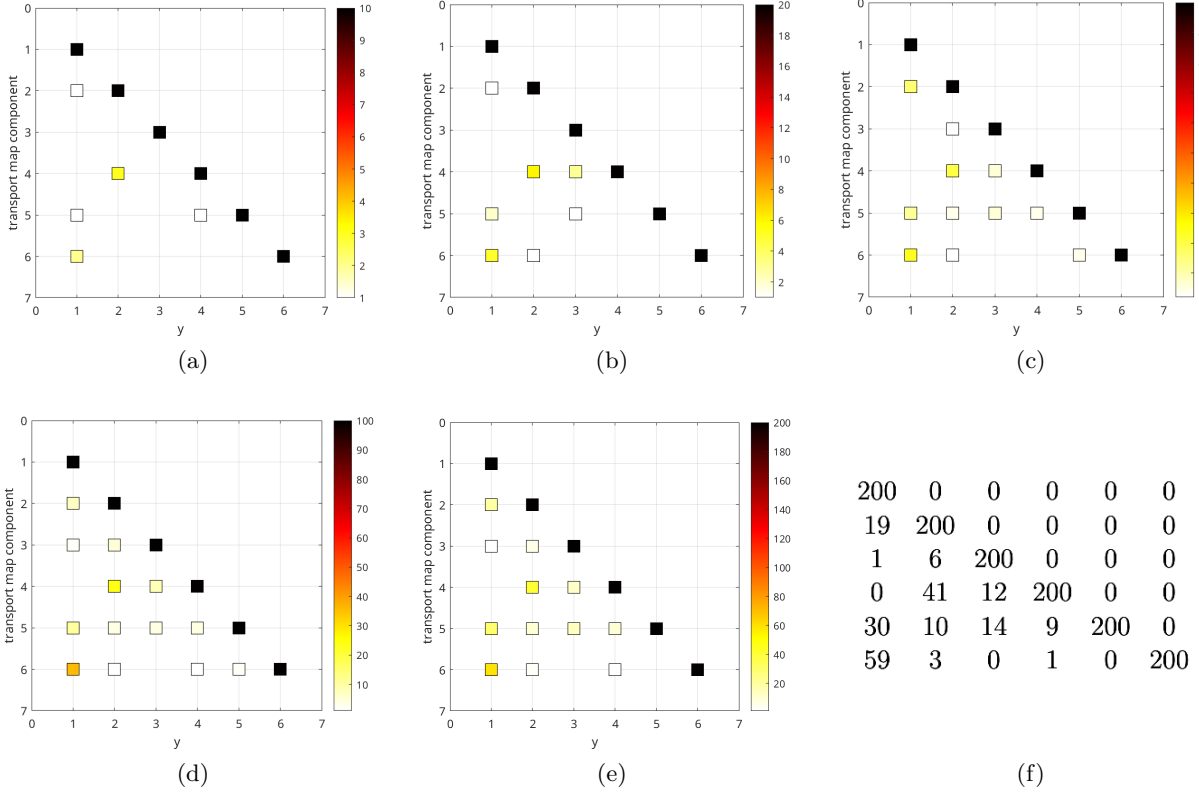


Figure 10: Aggregated sparsity patterns from adaptive transport map approximations to data distributions for different subsets of the zero-dose radiation data samples. Subsets consisting of half the number of total samples (which for the zero-dose radiation class is 18) were generated from random permutations of the GSE43151 data set sample ordering. In subplots 10a, 10b, 10c, 10d, and 10e, there are, respectively, 10, 20, 50, 100, and 200 such subsets represented. By aggregating results for increasing numbers of data subsets, high-frequency sparsity patterns are seen to emerge and persist. We note that the groups of runs represented in subplots 10a–10e were independent, so low-frequency sparsity patterns need not persist as we move from subplot 10a to subplot 10e. This was the case for grid point (5,6) in subplots 10d and 10e, which shows a two-frequency dependency on the value y_5 of the random variable \mathcal{J}_5 for map component $(T^{-1})_6$ in subplot 10d, but zero-frequency dependency in subplot 10e. For reference, subplot 10f shows the frequency values corresponding to the sparsity pattern from subplot 10e.

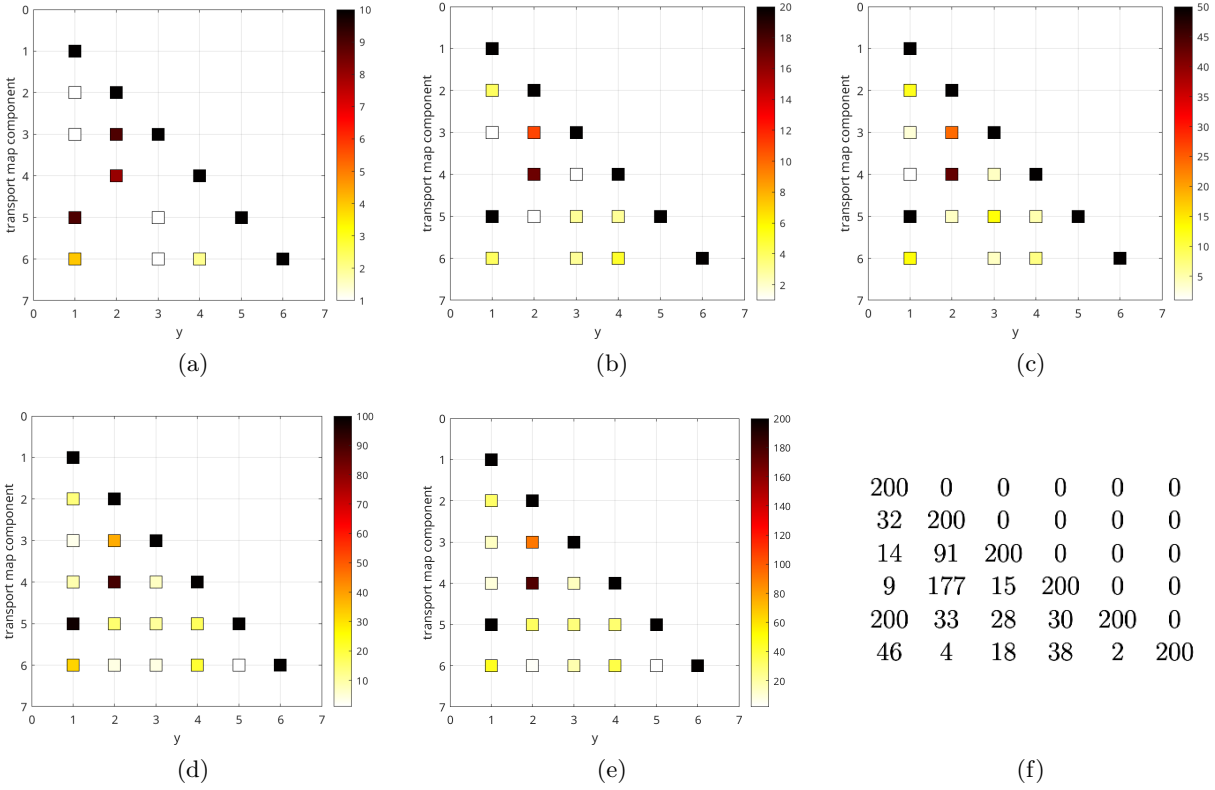


Figure 11: Aggregated sparsity patterns from adaptive transport map approximations to data distributions for different subsets of the low-dose radiation data samples. Subsets consisting of half the number of total samples (which for the low-dose radiation class is 87) were generated from random permutations of the GSE43151 data set sample ordering. In subplots 10a, 10b, 10c, 10d, and 10e, there are, respectively, 10, 20, 50, 100, and 200 such subsets represented. As for the zero-dose radiation class in Figure 10, by aggregating results for increasing numbers of data subsets, high-frequency sparsity patterns are seen to emerge and persist. For reference, subplot 11f shows the frequency values corresponding to the sparsity pattern from subplot 11e.

Computing frequency results from larger collections of subsets, as in Figures 10a-10e for the zero-dose radiation class and Figures 11a-11e for the low-dose one, we observe that high-frequency patterns (pointing to particular subsets of random variables) start to emerge and persist. We note that a larger collection of subsets need not contain the smaller collection of subsets from previous frequency counts – that is the case in Figures 10 and 11. Such high-frequency patterns are suggestive of gene relationships encoded (or hidden) in the data which, as we have already mentioned, may aid in hypothesis generation for subsequent validation. An example is shown in Figure 12. We believe that these initial results show promise and deserve further investigation.

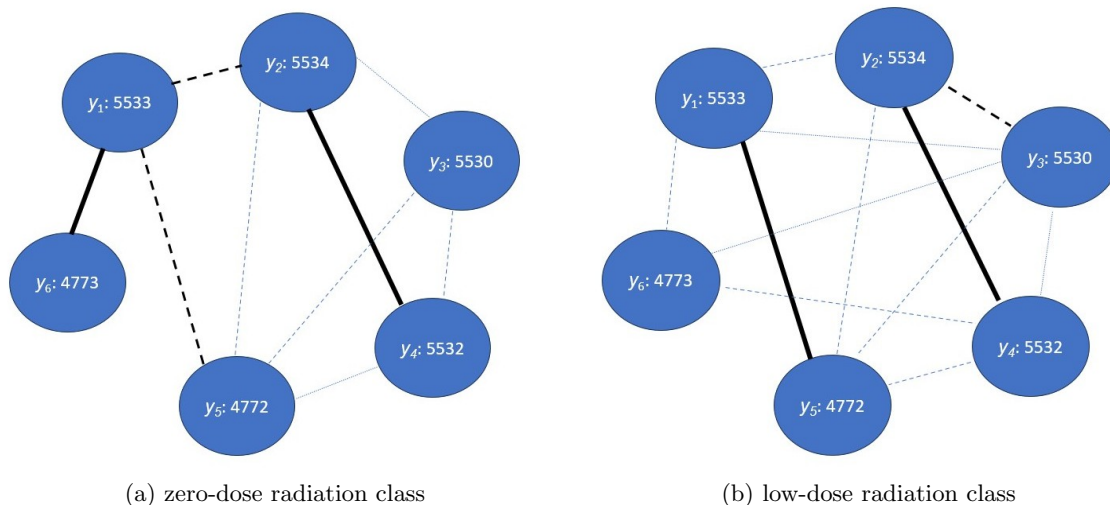


Figure 12: *Subplot 12a*: Dependencies among the random variables $\{\mathcal{Y}_k\}_{k=1}^6$ for the zero-dose radiation class, as implied by the sparsity pattern from Figure 10e. *Subplot 12b*: Dependencies among the random variables $\{\mathcal{Y}_k\}_{k=1}^6$ for the low-dose radiation class, as implied by the sparsity pattern from Figure 11e. Each random variable is identified with a gene, per the gene label ids in the GSE43151 data set. A natural question is whether the above reveal biological information, such as relationships among genes with no radiation exposure that change (appear, disappear) or persist upon exposure to low-dose radiation.

While more extensive research is warranted, the work reported in this manuscript shows some of the benefits that measure transport techniques will provide as part of the computational workflow from Section 2, intended to support research in the biological sciences. In domains for which data scarcity is common, such as in the radiation biology case study from Section 5, engagement with domain scientists will aid in identifying types of prior knowledge (in addition to biological pathway knowledge) which can be incorporated into the formulation of the mathematical problems being solved. This should allow to better account for the scarcity of training data. How to incorporate prior knowledge will obviously depend on the type of prior knowledge and problem being addressed but, generally, we mention feature selection for model training as well as incorporation of additional constraints in optimization problems being solved as common approaches. This is also among the topics of our ongoing work.

Acknowledgements

This work was supported by the U.S. Department of Energy, Office of Science, RadBio program under Award KP1601011/FWP CC121.

VLM thanks Francis J. Alexander who, as a RadBio PI, supported the measure transport approach, as well as for helpful discussions while the research was being carried out. VLM also thanks Ognyan Stoyanov for helpful discussions on measure transport theory and for feedback on preliminary versions of this manuscript, Ricardo Baptista for helpful discussions on adaptive transport maps and the TransportMaps library, Daniel Sharp for helpful discussions on the MParT library, and Shinjae Yoo and Shantenu Jha for some managerial support.

References

- [1] J. P. Agnelli, M. Cadeiras, E. G. Tabak, C. V. Turner, and E. Vanden-Eijnden. Clustering and classification through normalizing flows in feature space. *Multiscale Modeling & Simulation*, 8(5):1784–1802, 2010. <https://doi.org/10.1137/100783522>.
- [2] Ricardo Baptista, Youssef Marzouk, and Olivier Zahm. On the representation and learning of monotone triangular transport maps, 2022. <https://arxiv.org/abs/2009.10303>.
- [3] Ricardo Baptista and Paul-Baptiste Rubio. AdaptiveTransportMaps software library. <https://github.com/baptistar/ATM>.
- [4] V. I. Bogachev, A. V. Kolesnikov, and K. V. Medvedev. Triangular transformations of measures. *Sbornik: Mathematics*, 196(3), 2005.
- [5] Shahin Boluki, Mohammad Shahrokh Esfahani, Xiaoning Qian, and Edward A. Dougherty. Incorporating biological prior knowledge for Bayesian learning via maximal knowledge-driven information priors. *BMC Bioinformatics*, 18, 2017. <https://doi.org/10.1186/s12859-017-1893-4>.
- [6] Laurent Dinh, Jascha Sohl-Dickstein, and Samy Bengio. Density estimation using Real NVP. 2017. <https://arxiv.org/abs/1605.08803>.
- [7] Ron Edgar, Michael Domrachev, and Alex E. Lash. Gene Expression Omnibus: NCBI gene expression and hybridization array data repository. *Nucleic Acids Research*, 30(1):207–210, 2002. <https://doi.org/10.1093/nar/30.1.207>.
- [8] Tarek A. El Moselhy and Youssef M. Marzouk. Bayesian inference with optimal maps. *Journal of Computational Physics*, 231(23):7815–7850, 2012. <https://doi.org/10.1016/j.jcp.2012.07.022>.
- [9] Marylou Gabri e, Grant M. Rotskoff, and Eric Vanden-Eijnden. Adaptive Monte Carlo augmented with normalizing flows. *Proceedings of the National Academy of Sciences*, 119(10), 2022. [10.1073/pnas.2109420119](https://doi.org/10.1073/pnas.2109420119).
- [10] Farzan Ghanegolmohammadi, Shinsuke Ohnuki, and Yoshikazu Ohya. Assignment of unimodal probability distribution models for quantitative morphological phenotyping. *BMC Biol*, 20, 2022. <https://doi.org/10.1186/s12915-022-01283-6>.
- [11] T. Hastie, R. Tibshirani, and J.H. Friedman. *The Elements of Statistical Learning: Data Mining, Inference, and Prediction*. Springer Series in Statistics. Springer, 2009.

- [12] The MathWorks Inc. Statistics and machine learning toolbox, 2022. <https://www.mathworks.com/products/statistics.html>.
- [13] Patrick R. Johnstone. https://github.com/1austrartsua1/KEGG_ML.
- [14] Minoru Kanehisa and Susumu Goto. KEGG: Kyoto Encyclopedia of Genes and Genomes. *Nucleic Acids Research*, 28(1):27–30, 2000. <https://doi.org/10.1093/nar/28.1.27>.
- [15] Matthias Katzfuss and Florian Schäfer. Scalable Bayesian transport maps for high-dimensional non-Gaussian spatial fields, 2023. <https://arxiv.org/abs/2108.04211>.
- [16] Markelle Kelly, Rachel Longjohn, and Kolby Nottingham. The UCI Machine Learning Repository. <https://archive.ics.uci.edu>.
- [17] A. V. Kolesnikov. Convexity inequalities and optimal transport of infinite-dimensional measures. *J. Math. Pures Appl.*, 83:1373–1404, 2004.
- [18] Volker Lohweg. Banknote Authentication. UCI Machine Learning Repository, 2013. DOI: <https://doi.org/10.24432/C55P57>.
- [19] Xihai Luo, Sean McCorkle, Gilchan Park, Vanessa López-Marrero, Shinjae Yoo, Edward R. Dougherty, Xiaoning Qian, Francis J. Alexander, and Byung-Jun Yoon. Comprehensive analysis of gene expression profiles to radiation exposure reveals molecular signatures of low-dose radiation response. In *2022 IEEE International Conference on Bioinformatics and Biomedicine (BIBM)*, pages 2366–2374. IEEE, 2022.
- [20] Xihai Luo, Seyednami Niyakan, Patrick Johnstone, Sean McCorkle, Gilchan Park, Vanessa López-Marrero, Shinjae Yoo, Edward R. Dougherty, Xiaoning Qian, Francis J. Alexander, Shantenu Jha, and Byung-Jun Yoon. Pathway-based analyses of gene expression profiles at low doses of ionizing radiation, 2023. *Submitted*.
- [21] Youssef Marzouk, Tarek Moselhy, Matthew Parno, and Alessio Spantini. Sampling via measure transport: An introduction. In Roger Ghanem, David Higdon, and Houman Owhadi, editors, *Handbook of Uncertainty Quantification*, pages 1–41. Springer International Publishing, Cham, 2016. https://doi.org/10.1007/978-3-319-11259-6_23-1.
- [22] Rebecca E. Morrison, Ricardo Baptista, and Youssef Marzouk. Beyond normality: Learning sparse probabilistic graphical models in the non-Gaussian setting. In *Proceedings of the 31st International Conference on Neural Information Processing Systems, NIPS’17*, pages 2356–2366, Red Hook, NY, USA, 2017. Curran Associates Inc.
- [23] Ingrid Nosel, Aurélie Vaurijoux, Joan-Francesc Barquineró, and Gaetan Gruel. Characterization of gene expression profiles at low and very low doses of ionizing radiation. *DNA Repair*, 12(7):508–517, 2013. <https://doi.org/10.1016/j.dnarep.2013.04.021>.
- [24] F. Otto and C. Villani. Generalization of an inequality by Talagrand, and links with the logarithmic Sobolev inequality. *Journal of Functional Analysis*, 173(2):361–400, 2000. <https://doi.org/10.1006/jfan.1999.3557>.
- [25] George Papamakarios, Eric Nalisnick, Danilo Jimenez Rezende, Shakir Mohamed, and Balaji Lakshminarayanan. Normalizing flows for probabilistic modeling and inference. *J. Mach. Learn. Res.*, 22(1), 2021. <https://dl.acm.org/doi/abs/10.5555/3546258.3546315>.

- [26] Gilchan Park, Byung-Jun Yoon, Xihaier Luo, Vanessa López-Marrero, Patrick Johnstone, Shinjae Yoo, and Francis Alexander. Automated extraction of molecular interactions and pathway knowledge using large language model, Galactica: Opportunities and challenges. In *The 22nd Workshop on Biomedical Natural Language Processing and BioNLP Shared Tasks*, pages 255–264, 2023.
- [27] Gilchan Park, Byung-Jun Yoon, Xihaier Luo, Vanessa López-Marrero, Patrick Johnstone, Shinjae Yoo, and Francis J. Alexander. Comparative performance evaluation of large language models for extracting molecular interactions and pathway knowledge. *arXiv preprint arXiv:2307.08813*, 2023.
- [28] Gabriel Peyré and Marco Cuturi. Computational optimal transport: With applications to data science. *Foundations and Trends[®] in Machine Learning*, 11(5-6):355–607, 2019. <http://dx.doi.org/10.1561/22000000073>.
- [29] F. Santambrogio. *Optimal Transport for Applied Mathematicians: Calculus of Variations, PDEs, and Modeling*. Progress in Nonlinear Differential Equations and Their Applications. Springer International Publishing, 2015. <https://doi.org/10.1007/978-3-319-20828-2>.
- [30] B.W. Silverman. *Density Estimation for Statistics and Data Analysis*. Monographs on Statistics and Applied Probability. Chapman & Hall, 1998.
- [31] Alessio Spantini, Ricardo Baptista, and Youssef Marzouk. Coupling techniques for nonlinear ensemble filtering. *SIAM Review*, 64(4):921–953, 2022. <https://doi.org/10.1137/20M1312204>.
- [32] Alessio Spantini, Daniele Bigoni, and Youssef Marzouk. Inference via low-dimensional couplings. *The Journal of Machine Learning Research*, 19(1):2639–2709, 2018.
- [33] E. G. Tabak and Cristina V. Turner. A family of nonparametric density estimation algorithms. *Communications on Pure and Applied Mathematics*, 66(2):145–164, 2013. <https://doi.org/10.1002/cpa.21423>.
- [34] Esteban G. Tabak and Eric Vanden-Eijnden. Density estimation by dual ascent of the log-likelihood. *Communications in Mathematical Sciences*, 8(1):217–233, 2010. [10.4310/CMS.2010.v8.n1.a11](https://doi.org/10.4310/CMS.2010.v8.n1.a11).
- [35] MIT Uncertainty Quantification Group. Software libraries. <https://uqgroup.mit.edu/software>.
- [36] MIT Uncertainty Quantification Group. TransportMaps software library. <https://transportmaps.mit.edu/docs/>.
- [37] C. Villani. *Optimal Transport: Old and New*. Springer Berlin, Heidelberg, 2009. <https://doi.org/10.1007/978-3-540-71050-9>.
- [38] Hongkang Yang and Esteban G. Tabak. Conditional density estimation, latent variable discovery, and optimal transport. *Communications on Pure and Applied Mathematics*, 75(3):610–663, 2022. <https://doi.org/10.1002/cpa.21972>.